Analyst

PAPER

View Article Online
View Journal

Cite this: DOI: 10.1039/d5an01058f

3D-printed hollow microneedle-based electrochemical sensor for wireless glucose monitoring

Chuchu Chen,†[a] Yonghao Fu,†[a] Yuehe Lin,[a] Yun Liu,[b] Dan Du *[a,c] and Kaiyan Qiu *[a]

Received 6th October 2025,
Accepted 30th December 2025

DOI: 10.1039/d5an01058f

rsc.li/analyst

Wearable electrochemical sensors have aroused tremendous attention due to their great potential for *in situ* and continuous assessment for glucose monitoring. The conventional fingerstick test is the easiest and most efficient method for glucose evaluation, but it is invasive and painful. Here we introduce a wearable and user-friendly microneedle-based electrochemical sensor, fabricated *via* resin 3D printing with an affordable desktop 3D printer and featuring a single-atom nanozyme-modified electrode, offering high sensitivity and superior selectivity for glucose monitoring. This minimally invasive electrochemical sensor demonstrates the capability to extract artificial interstitial fluid using hollow microneedles and a finger-activated pump, enabling continuous monitoring of dynamic glucose concentration changes. This electrochemical sensor exhibits remarkable sensitivity and selectivity, with a linear range of 0.1 μM to 50 mM and a limit of detection of 0.285 μM, attributed to the incorporation of single-atom nanozymes with peroxidase-like enzymatic activity. The glucose concentration data are wirelessly transmitted to a smartphone application in real time, offering user-friendly access and facilitating remote monitoring. The described electrochemical sensor presents the possibilities for point-of-care health monitoring applications.

Introduction

Diabetes is a widely spread chronic metabolic disorder.[1,2] Glucose is the most important risk indicator of diabetes, and strict glycemic control and continuous glucose monitoring have been proven remarkable in reducing the deterioration of diabetes and preventing secondary complications.[3,4] Continuous glucose monitoring can provide accurate and reliable glucose measurements in real time.[5,6] Traditional fingerstick glucose sensing is invasive and painful, inevitably causing damage to the skin if tested 6 to 8 times a day.[7] To address these challenges, various wearable noninvasive or minimally invasive sensors have emerged as promising alternatives for continuous glucose monitoring.[8,9] These devices leverage advanced technologies such as optical,[10,11] thermal,[12,13] and transdermal electrochemical techniques,[14,15] offering high versatility. Despite their potential, they still face limitations, including sensitivity, selectivity, biocompatibility and user convenience.[16]

Interstitial fluid (ISF), particularly present in the dermal layer of the skin, has a similar composition profile to blood due to its capability to exchange substances between the cells and blood by diffusion,[17,18] making it a valuable candidate for glucose monitoring.[19] Despite being promising, obtaining ISF is still challenged by the minuscule volumes available in the dermis (120 μL cm^{-2}) and the filtration effect caused by the applied force, leading to slow extraction rates for continuous sampling.[20,21] Microneedles (MNs) have been used for drug delivery and transdermal extraction.[22–24] The length of the MNs is generally between 100 and 1000 μm, which can guarantee that MNs can puncture the stratum corneum without stimulating the nerves and vessels in the dermis for painless and minimally invasive effects.[19,25] Hollow microneedles (HMNs) have been reported to sample ISF *via* epidermis piercing and capillary force for glucose monitoring.[26,27] To date, the combination of micropores and the suction approach has improved the collection rate over sole needle-based extraction and reduced tissue damage caused by suction blisters.[21,28,29]

Nanozymes, nanomaterials with enzyme-like activities, have been developed as efficient catalysts by researchers due to the

[a]School of Mechanical and Materials Engineering, Washington State University, Pullman, Washington 99164, USA. E-mail: kaiyan.qiu@wsu.edu, annie.du@wsu.edu
[b]Research School of Chemistry, Australian National University, Canberra, ACT 2601, Australia
[c]Department of Pharmaceutical Sciences, College of Pharmacy and Pharmaceutical Sciences, Washington State University, Spokane, Washington 99202, USA
† These authors contributed equally to this work.

advantages of low cost, ultrahigh activity, high stability and so on.[30,31] Single-atom nanozymes (SANs), a class of nanozymes characterized by atomically dispersed active sites, exhibit enzyme-like activity and chemical stability, endowing them with unique catalytic performance.[32–36] Recently, Fe-based SANs with dispersed Fe atoms, known as Fe–N–C-based SANs, have shown superior peroxidase-like characteristics.[37] The superior catalytic performance of Fe–N–C SANs for hydrogen peroxide (H_2O_2) makes them widely used in various sensor applications, such as the detection of glucose, uric acid, lactate, herbicide and butyrylcholinesterase, as reported in our previous studies.[38–40]

Herein, we present a novel wearable electrochemical sensor for glucose monitoring in ISF. Compared with previous glucose sensors, our study introduces an innovative combination of 3D-printed HMNs and SANs to address the key limitations in existing technologies. HMNs are fabricated using commercially available bio resin with an affordable desktop 3D printer (costing less than $600), significantly reducing the cost of HMN-based biosensors.[41–43] The HMNs allow minimally invasive sampling for ISF and ensure safe interaction with the skin without irritation and toxicity concerns. The integration of 3D-printed HMNs and a finger-activated pump demonstrates the ISF extraction capability in a minimally invasive approach, which is validated through the sampling of artificial ISF from a skin-mimicking phantom gel. In addition, the incorporation of SANs significantly boosts the sensitivity and selectivity of electrochemical sensing, offering a low limit of detection (LOD) of 0.285 μM for glucose within a wide detection range of 0.1 μM–50 mM. Furthermore, the sensor is coupled with a potentiostat, enabling real-time and wireless data transmission to a smartphone application to provide immediate results of glucose levels. Beyond glucose detection, this versatile platform holds great potential for expanding the detection of a wide range of biomarkers in ISF. This research aims to develop and validate the wireless sensor, showcasing its sensitivity and selectivity using a skin-mimicking phantom gel, thereby laying the foundation for future advancements in wearable biosensors.

Experimental

Fabrication of HMNs and a pump using resin 3D printers

HMNs (5 × 5 array) and an elastic pump were fabricated using Anycubic bio resin on a resin 3D printer (Anycubic Photon Mono M5s Pro, Anycubic Technology Co., Shenzhen, China) and Elastic 50A Resin V2 (Form 3) on Form 3+ printer (Formlab, Somerville, MA, USA), respectively. The HMN arrays and pump were designed in AutoCAD software (Fusion 360, Autodesk, USA) and exported to .STL format files. The HMN model files were subsequently rotated by 45 degrees along both the *X* and *Y* axes for optimized supports and sliced using Anycubic Photon Workshop software, while the pump was auto-oriented and sliced by PreForm software. After the 3D printing process was complete, the prints were removed from the build platform and cleaned with an isopropyl alcohol solution to wash off residual resin. These prints were post-cured in a UV curing machine (λ = 405 nm) for solidification, followed by the removal of model supports.

Morphological characterization of HMNs

HMNs were coated with 10 nm thick gold and characterized by scanning electron microscopy (SEM) with a FEI SEM Apreo Volumescope. SEM imaging of the HMNs was used to image the morphology of the HMNs after fabrication and the HMN tip deformation during compression and parafilm penetration tests.

Mechanical and penetration tests of HMNs

The compression tests and parafilm penetration tests were performed using an Instron universal testing machine (Instron, model 600DX-C4A-G7G, Canton, MA, USA). The compression tests were used to examine the mechanical strength and the parafilm penetration tests were used to evaluate the penetration efficiency of the 3D-printed HMNs.[44] HMN patches were placed on the test platform with the tips upward, and a vertical force was applied at a moving speed of 1 mm min^{-1}. The loading force against displacement data was recorded during the test until the maximum force of 50 N was reached. For the parafilm penetration tests, HMN patches were placed on the top of the eight-layer parafilm (127 μm thickness per sheet) with the tip facing down, and the vertical force was applied to the HMNs at a load rate of 1 mm min^{-1}. When the loading force reached 40 N, the ramp speed was reduced to 0 mm min^{-1} and the force was maintained for 30 s.[45] After that, the HMNs were removed and the parafilm sheets were separated to count the holes created on each layer. These mechanical tests were repeated 3 times. The penetration efficiency was calculated according to the ratio of holes generated in each layer using the following equation:[46]

$$\text{Hole created (\%)} = (\text{number of holes observed}/\text{number of HMN}) \times 100.$$

Preparation of Fe–N–C SANs

The preparation of Fe–N–C SANs was based on our previous reports.[47] 100 mg of $Fe(NO_3)_3{\cdot}9H_2O$ was introduced into 160 mL of methyl alcohol containing 3.39 mg of $Zn(NO_3)_2{\cdot}6H_2O$ with intense ultrasound for 30 min. Following this, another 160 mL of methyl alcohol solution containing 3.94 g of 2-methylimidazole (2-MeIM) was added to the above solution. Then, the above mixture was sealed in an Erlenmeyer flask, shaken for 1 min and allowed to stand overnight at 60 °C. Fe-doped zeolitic imidazolate framework-8 (ZIF-8) was collected after centrifugation at 7000 rpm (Eppendorf Centrifuge 5804 R, Germany) for 10 min and washed three times with deionized water and ethyl alcohol, respectively. Fe–N–C SANs were obtained from a pyrolytic process of Fe-doped ZIF-8 at 900 °C (Across International STF 1200 Tube Furnace, USA) under a nitrogen atmosphere for 30 min, followed by an ammonia atmosphere for 30 min. Fe–N–C SANs were washed

with 2 M of HCl at 60 °C for 6 h. Finally, the Fe–N–C SANs were dried in a freeze dryer (FreeZone 4.5 Liter-50C benchtop freeze dryer) and stored away from light for later use.

Characterization of Fe–N–C SANs

The morphology and structure of Fe–N–C SANs were obtained using transmission electron microscopy (TEM) with an FEI Tecnai G2 20 Twin TEM operated at 200 kV and equipped with a LaB_6 electron source. High-angle annular dark-field scanning transmission electron microscopy (HAADF-STEM) was performed using a Hitachi HD2700C microscope operating at an accelerating voltage of 200 kV. The instrument is equipped with a probe aberration corrector, offering a spatial resolution of <1 Å and an energy resolution of 0.35 eV. The collection angle ranges from 64 to 341 mrad for HAADF.

Based on the protocol from previous studies, the enzyme activity of Fe–N–C SANs was measured and calculated.[48,49] For peroxidase-like activity, 10 μL of 10 mg mL^{-1} 3,3′,5,5′-tetramethylbenzidine (TMB) solution and 1 μL of 1 M H_2O_2 solution were added to 88 μL of 0.2 M sodium acetate–acetic acid buffer (pH = 4.0). Subsequently, 1 μL of 0.02 mg mL^{-1} Fe–N–C SAN dispersion was introduced and mixed thoroughly. The absorbance at 652 nm was monitored every 10 s over a 10 min period. For evaluation of oxidase-like activity, the same procedure was followed, except that H_2O_2 was not added. All experiments were conducted at 37 °C. The enzyme activity was calculated using the following equation:

$$U = \frac{V}{\varepsilon l} \times \frac{\Delta A}{\Delta t}$$

where U is the enzyme activity (U), V is the total reaction solution volume, ε is the molar adsorption coefficient of the TMB substrate (39 000 L mol^{-1} cm^{-1} at 652 nm), l is the optical path length of the reaction system (cm), and $\Delta A/\Delta t$ (min^{-1}) is the rate of the absorbance change during the initial 1 min.

Electrochemical analysis was performed using cyclic voltammetry (CV) and amperometry methods with a CHI660E series electrochemical workstation (CH Instruments, Inc., Austin, USA). Firstly, screen-printed electrodes (SPEs) were activated using the CV method in 0.1M PBS (pH = 7.4) solution over a potential range from −2.5 V to 2.5 V at a scan rate of 100 mV s^{-1} for 15 cycles. 5 mg of Fe–N–C SANs were thoroughly dispersed in a mixed solution containing 990 μL of PBS and 10 μL of 1 wt% Nafion to prepare a 5 mg mL^{-1} Fe–N–C SAN ink (hereinafter referred to as "ink"). 4 μL of 5 mg mL^{-1} ink was added dropwise onto the working electrode (WE) surface of the SPE, and the electrode was then dried at room temperature to obtain the SAN-modified SPE. The bare SPE was immersed in 10 mL of 0.01 M phosphate-buffered saline (PBS) containing 0 and 2.5 mM H_2O_2 for electrochemical analysis using CV. Similarly, 10 mL of 0.01 M PBS containing 0, 1.25, 2.5 and 3.75 mM H_2O_2 was measured with a SAN-modified SPE using the CV method. The CV measurements were conducted over a potential range from −1.0 V to 0.6 V at a scan rate of 50 mV s^{-1}. Amperometry was used to analyze the continuous response of the SAN-modified SPE to increasing concentrations of H_2O_2. Amperometry measurement was performed at a potential of −0.2 V using the SPE. First, the SAN-modified SPE was immersed in 100 mL of continuously stirred 0.01 M PBS solution without H_2O_2. To simulate increasing concentrations, 50 μL of 200 mM H_2O_2 (prepared in PBS) was manually added to the stirred solution using a pipette. Each addition was performed only after the current signal stabilized, ensuring accurate measurement of the response to each incremental concentration. The corresponding current change over time was recorded. The above electrochemical data were all smoothed and analyzed using CHI660e software.

Preparation and detection performance of Fe–N–C SAN-modified SPEs

SAN-modified SPEs, prepared as described in the "Characterization of Fe–N–C SANs" section, were immersed in 2 mg mL^{-1} glucose oxidase (GOx) solution for 24 h to obtain SAN/GOx-modified SPEs. Meanwhile, the SPEs without SANs were also immersed in 2 mg mL^{-1} GOx solution for 24 h to obtain GOx-modified SPEs. The bare SPE, GOx-modified SPE, SAN-modified SPE and SAN/GOx-modified SPE were analyzed in a 2.5 mM glucose solution using the CV method with a CHI660E electrochemical workstation. The CV settings were the same as those described in the "Characterization of Fe–N–C SANs" section. The amperometry method was applied for glucose detection at −0.22 V using a CHI660E electrochemical workstation. D-Glucose was dissolved in 0.01 M PBS (pH = 7.4) to prepare glucose solutions with a concentration range of 0.1 μM to 50 mM for the calibration curve. 70 μL of glucose solution was added dropwise onto the surface of three electrodes (WE, counter electrode and reference electrode) of the SAN/GOx-modified SPE to obtain the response currents at −0.22 V to varying glucose concentrations. Then, 5 mM uric acid, L-alanine, lactate, and ascorbic acid were prepared for the interference test. 70 μL of interference solution was added onto the SAN/GOx-modified SPE to analyze the response current using amperometry at −0.22 V. Seven identical SAN/GOx-modified SPEs were made using the same method and then tested with 2 mM glucose solution using amperometry. Meanwhile, the SAN/GOx-modified SPEs were stored at 4 °C and room temperature for one month and tested with 1 mM glucose solution using amperometry every week. All the above results obtained from the electrochemical workstation were smoothed and analyzed using CHI660e software.

Glucose detection in artificial ISF

To prepare artificial ISF, 2.5 mM $CaCl_2$, 5.5 mM glucose, 10 mM HEPES, 3.5 mM KCl, 0.7 mM $MgSO_4$, 123 mM NaCl, 1.5 mM NaH_2PO_4, and 7.4 mM saccharose were dissolved in Milli-Q water and the pH value was adjusted to 7.0 using HCl solution.[50–52] All chemicals were used without further modification and purification. Artificial ISF solutions with varying glucose concentrations were prepared by spiking glucose into artificial ISF for subsequent detection. Glucose detection in artificial ISF was conducted using an ECWP110plus wireless potentiostat (Zensor R&D co., Ltd). The potentiostat device

consists of a remote and a connector. The SAN/GOx-modified SPE was inserted into the connector, while the remote was connected to the USB port of a computer. The connector collected the electric signal from the SPE and transmitted the signal to the computer *via* the remote. The amperometric method was applied to analyze the signal from the connector using EIWP110 software (Zensor R&D co., Ltd) on the computer. The operation interface is displayed in Fig. S1. As shown in Fig. S1A and B, the potential was set to −0.22 V to obtain the response currents, which were used to create the standard curve correlating current with glucose concentration in ISF. In Fig. S1C, the standard curve equation was entered into the software for subsequent detection. The above method was also applied to continuous glucose detection in ISF. To perform continuous detection, the glucose solution was added to the ISF solution to achieve a continuous increase of glucose concentration in 100 mL of ISF solution. During continuous measurement, concentrations of glucose were 0.98, 5.98, 10.60 and 20.05 mM, respectively. After adding glucose solution in artificial ISF, the magnetic bead was constantly stirred in the ISF solution to quickly reach the target glucose concentration. The amperometry curve was generated after analysis using EIWP110 software. The glucose concentration was then calculated using the pre-entered equation and displayed on the computer software interface. Meanwhile, the result was sent wirelessly and displayed on the smartphone application ECWP (Zensor R&D co., Ltd).

Evaluation in a skin-mimicking phantom gel

To simulate the mechanical properties of human skin, a skin-mimicking phantom gel was prepared and used to evaluate the electrochemical performance of the sensor.[53] A 1.4% agarose gel was prepared by mixing 140 mg of agarose into 10 mL of the aforementioned artificial ISF. The mixture was continuously stirred at 120 °C until it became completely clear. Subsequently, the solution was poured into round-shaped molds to solidify at room temperature. To further mimic skin, a layer of parafilm was placed over the prepared gel.[27] During the phantom hydrogel experiments, the HMNs of the sensor penetrated through the parafilm into the phantom gel. The HMNs remained in contact with the gel for 1 min before the electrochemical detection of glucose.[54] This setup verified the ISF sampling ability and the electrochemical sensitivity of the integrated sensor. The same method used for glucose detection in ISF was applied to detect glucose concentration in a skin-mimicking phantom gel. The signal from the connector was analyzed by amperometry using EIWP110 software. Once the current stabilized, the gel with a certain concentration of glucose was replaced with the gel containing a different glucose concentration. Glucose ISF solutions of 1, 2, 5, 10, 15 and 20 mM were detected in a skin-mimicking phantom gel. The result was sent to a smartphone application after software analysis using amperometry. In addition, the stability and repeatability of the finger-activated pump were evaluated by quantifying the extracted volume per actuation. Prior to testing, the integrated sensing platform was completely dried at room temperature to eliminate moisture interference during volume measurement. After each actuation, the pump extracted ISF analog through HMNs from the skin-mimicking phantom gel. The sensing platform was weighed to determine the mass change, which was then converted to volume. The extraction experiment was performed 30 times to assess sampling repeatability. Meanwhile, the pump was actuated 100 times to evaluate the mechanical durability and operational stability.

Results and discussion

Design of a 3D-printed HMN-based electrochemical sensor

As illustrated in Fig. 1A, the 3D-printed HMN-based electrochemical sensor includes three key components: (1) a touch-activated pump to enhance fluid extraction, (2) a SAN-functionalized SPE for *in situ* and real-time electrochemical glucose analysis, and (3) a 3D-printed HMN array for minimal invasive extraction of ISF. The flexible and soft 3D-printed pump (inner chamber volume: 232.8 cm^3) is incorporated to create negative pressure by finger pressing to facilitate the sampling of ISF through the HMNs and transport it to the surface of the sensing area. Once the finger load is removed, the pump can self-recover to the initial state. The WE (area: 7.1 mm^2) of SPE is functionalized by SANs for the sensitive detection of glucose in ISF. The SPE is stabilized between the pump and HMN patch by two-part epoxy adhesive (Loctite® Epoxy Clear Multi-Purpose, Henkel). Two circular holes (1 mm in diameter) are pre-punched between the electrodes, serving as channels to generate negative pressure inside the HMNs. The fabrication process, as shown in Fig. 1B, comprises three steps: (1) modify the WE of the SPE with SANs; (2) punch two circular holes between three electrodes; and (3) attach the HMNs and the pump with adhesive to both sides of the SPE. During measurement, the SPE is connected to a finger-sized potentiostat, where the electrochemical signals are recorded as electric signals and wirelessly transmitted. The glucose concentration results are displayed on a smartphone application for real-time health monitoring.

Synthesis and characterization of Fe–N–C SANs

The preparation of Fe–N–C SANs was based on the previous reports.[38,47] The synthesis schematic diagram is shown in Scheme 1. Briefly, the ZIF-8, a class of metal–organic frameworks, was synthesized from $Zn(NO_3)_2$ and 2-methylimidazole. Subsequently, $Fe(NO_3)_3$-doped ZIF-8 (ZIF-8@$Fe(NO_3)_3$) was prepared using ZIF-8 as precursor and $Fe(NO_3)_3$ as the dopant source. The Fe–N–C SANs were then obtained after pyrolysis at 900 °C. The transmission electron microscopy (TEM) image shows the characterization results of the Fe–N–C SANs (Fig. 2A). Fe–N–C SANs of similar shape and size (rhombic dodecahedral) were observed in the TEM image. Fig. 2B displays a HAADF-STEM image of Fe–N–C SANs. Bright dots are observed in images, representing dispersed Zn and Fe atoms. This phenomenon is attributed to the *Z*-contrast between

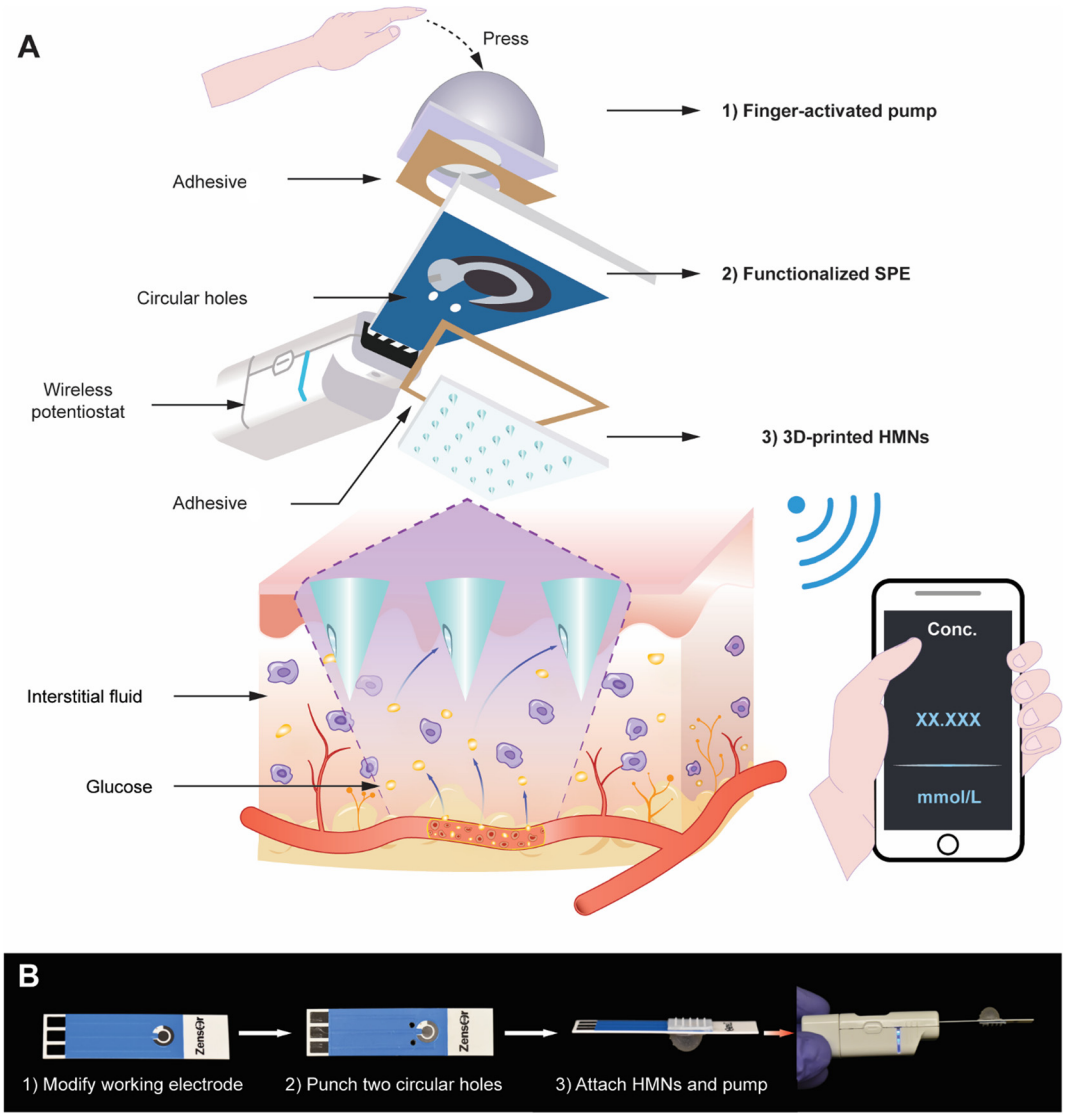

Fig. 1 Concept of the 3D-printed HMN-based electrochemical sensor. (A) Schematic illustrating the exploded view of the sensor and (B) fabrication procedures of the integrated sensor.

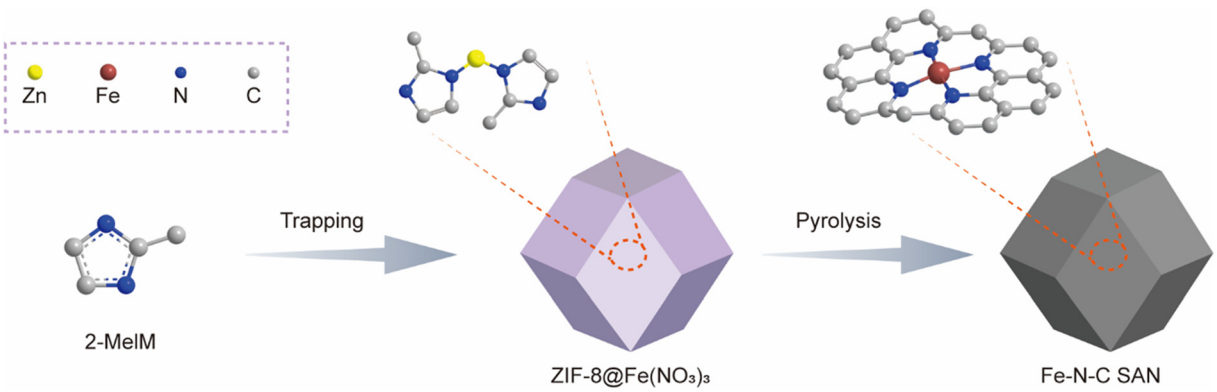

Scheme 1 The synthesis schematic diagram of Fe–N–C single-atom nanozymes. 2-Melm: 2-methylimidazole. ZIFs: zeolitic imidazolate frameworks. SAN: single-atom nanozyme.

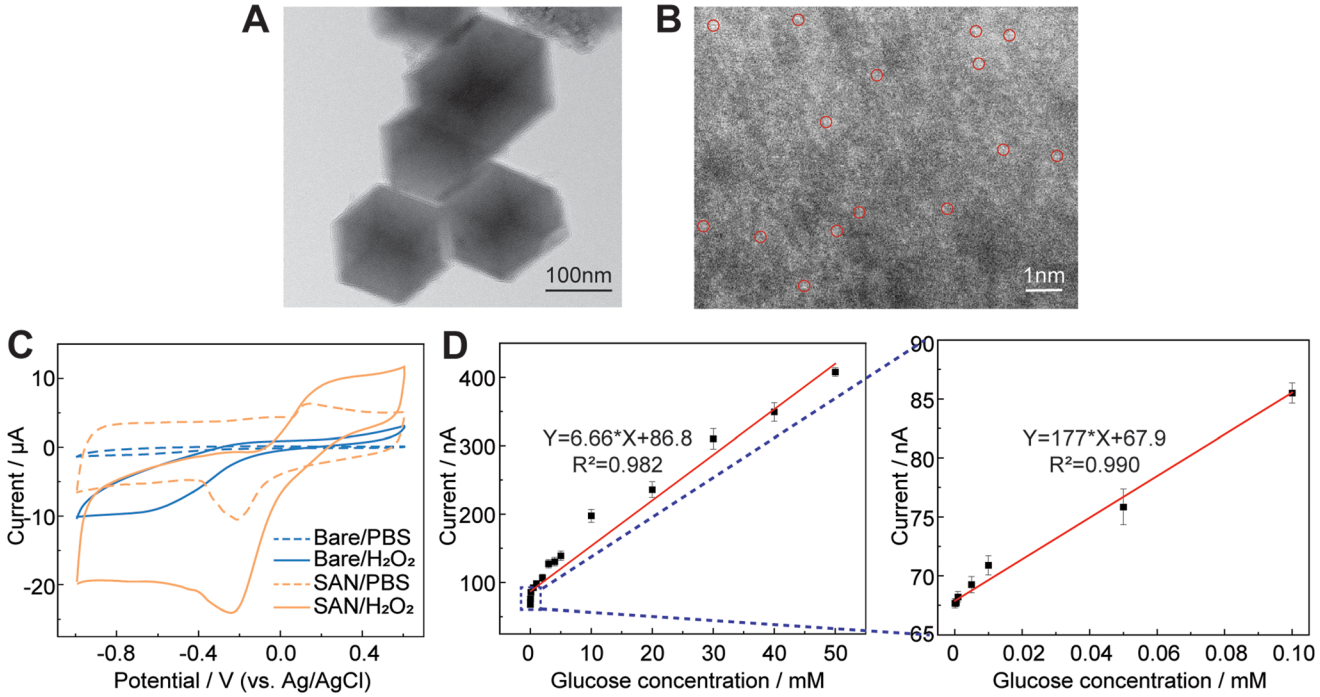

Fig. 2 Characterization and performance of Fe–N–C SANs. (A) TEM image of the Fe–N–C SAN structure; (B) HAADF-STEM image of Fe–N–C SANs. The circled bright dots are ascribed to the dispersed Zn and Fe atoms; (C) CV curves of bare and SAN-modified SPE in PBS solution with or without 2.5 mM H_2O_2; and (D) the standard curve for glucose detection on the SAN/GOx-modified SPE. The left panel shows the detection range of 0.1 μM–50 mM with the standard curve fitted from 0.1 mM to 50 mM, while the right panel shows the detection range of 0.1 μM–0.1 mM with the standard curve fitted exclusively for this range. All data are shown as mean ± SD (n = 3).

metal and carbon. The single-atom feature of SANs, demonstrated by the dispersed Zn and Fe in HAADF-STEM image, is key to their peroxidase-like activity. Fig. S2A shows the absorbance-time curves of TMB chromogenic reaction catalyzed by Fe–N–C SANs in the presence or absence of H_2O_2. As the reaction time increased, the absorbance at 652 nm increased gradually over 600 s. Notably, a significant linear relationship was observed between absorbances and reaction time within the first 60 s. By selecting the initial 60 s as the linear phase, the peroxidase-like and oxidase-like activity were calculated to 64.62 U mg^{-1} and 20.79 U mg^{-1}, respectively, as shown in Fig. S2B. The peroxidase-like activity of Fe–N–C SANs is higher than that of commonly used peroxidase-like nanozyme, such as Fe_3O_4, gold nanoparticles and carbon nanoparticles.[48,55]

Electrochemical performance of Fe–N–C SANs

The CV method was employed to evaluate the electrocatalytic performance of Fe–N–C SANs to H_2O_2. The Fe–N–C SANs were loaded onto SPE at a density of 0.28 mg cm^{-2}. The CV curves of bare SPE and Fe–N–C SAN-modified SPE in the presence and absence of 2.5 mM H_2O_2 in 0.01 M PBS (pH = 7.4) are shown in Fig. 2C. No significant peak was observed in the CV curve of the bare SPE in PBS (labeled bare/PBS), while a weak reduction peak appeared at −0.64 V in the presence of H_2O_2 (labeled Bare/H_2O_2), indicating that the reduction peak originates from the electrochemical reduction of H_2O_2. In contrast, the CV curve of the SAN-modified SPE in PBS (labeled SAN/PBS) showed a distinct reduction peak at −0.2 V, which was absent in the bare electrode, suggesting this signal results from the intrinsic redox activity of the Fe–N–C SANs. Furthermore, the CV curve of the SAN-modified SPE in the presence of H_2O_2 (labeled SAN/H_2O_2) exhibited an enhanced reduction peak at −0.2 V with a significantly increased current compared to that of SAN/PBS. This shift from the typical reduction potential of H_2O_2 (−0.64 V) to −0.2 V demonstrates the catalytic role of Fe–N–C SANs, which facilitates electron transfer and enables more efficient H_2O_2 reduction. This catalytic enhancement effectively reduces the overpotential by 0.44 V, indicating improved electrocatalytic activity toward H_2O_2 and contributing to enhanced selectivity by minimizing interference from other electroactive species. Fig. S3 shows the CV curves of Fe–N–C SAN-modified SPE in PBS with increasing concentration of H_2O_2 (1.25, 2.5, and 3.75 mM). As the concentration increases, the reduction peak current increases correspondingly, indicating that H_2O_2 is catalytically reduced by the Fe–N–C SANs.

The continuous H_2O_2 detection is shown in Fig. S4. Fig. S4A shows the amperometry curve of Fe–N–C SAN-modified SPE during the continuous addition of H_2O_2 in PBS solution at an applied potential of −0.2 V. With the addition of H_2O_2 solution, the response current increased gradually, which demonstrates the catalytic performance of Fe–N–C SANs. The concentration of H_2O_2 in the system after adding H_2O_2 was recorded, and a linear relationship between H_2O_2

concentration and response current is shown in Fig. S4B. The results indicate that the Fe–N–C SANs can be used for real-time and continuous detection of H_2O_2 by the electrochemical method and the extremely high R^2 value (0.998) also reflects the accuracy of the detection.

Detection performance of an Fe–N–C SAN-modified SPE

Fe–N–C SANs, with their intrinsic peroxidase-like activity and efficient catalytic performance toward H_2O_2, have emerged as potential modified nanomaterials in electrochemical biosensors.[37,56] Based on our previous findings,[57,58] we further advanced their application by integrating Fe–N–C SANs with GOx on an SPE to form a 3D-printed electrochemical biosensing platform. In this platform, GOx catalyzes the oxidation of glucose to gluconolactone, releasing H_2O_2, which is then catalytically reduced by Fe–N–C SANs.[59] Therefore, Fe–N–C SANs and GOx were immobilized on the SPE to construct an electrochemical biosensing platform in this study. Fig. S5 shows the electrochemical response of SPEs with different modifications to 2.5 mM glucose, measured using the CV method. Notably, a significant reduction peak was observed at −0.22 V for the SAN/GOx-modified SPE, indicating efficient electrocatalytic reduction of H_2O_2 generated from glucose by Fe–N–C SANs, thereby enabling sensitive glucose detection at a low potential. In Fig. 2D, amperometric measurement was performed on the electrode for the detection of glucose at −0.22 V in PBS (0.1 M, pH = 7.4). The detection range of glucose sensing is from 0.1 μM to 50 mM, where a linear relationship between the concentration of glucose and responding current is observed from 0.1 mM to 50 mM, following the equation $Y(\text{nA}) = 6.66 \times X(\text{mM}) + 86.8$ and an R^2 value of 0.982. Besides this, another linear relationship was also observed, following the equation $Y(\text{nA}) = 177 \times X(\text{mM}) + 67.9$ and an R^2 value of 0.990, ranging from 0.1 μM to 0.1 mM. The LOD was calculated according to the IUPAC-recommended approach, using the standard deviation of blank measurements (n = 7) and the calibration slope.[60] Specifically, the signal-domain threshold was defined as $I_{\text{LOD}} = \mu_b + 3.3 \times \sigma_b$, and the corresponding concentration-domain LOD was obtained by substituting this threshold into the calibration equation, yielding 0.285 μM. The LOD of the SAN/GOx-modified SPE demonstrates a lower LOD compared with most enzymatic and non-enzymatic electrochemical glucose sensors reported in the literature (Table S1), showing an enhancement of SANs for the sensitivity of glucose detection. In addition, the linear ranges and LODs of recently developed MN-based glucose sensors are summarized in Table S2. Notably, the sensor developed in this study exhibits a lower LOD and a broader detection range compared to most MN-based sensors. For the practical application of glucose biosensors, anti-interference, reproducibility and stability are very crucial.[61] Glucose sensing is affected by other substances in ISF.[62,63] Therefore, the response currents of glucose and various interfering substances, including uric acid, L-alanine, lactate and ascorbic acid, at the same concentration (5 mM) were tested to investigate whether interference would affect glucose detection. Fig. S6A shows the ratio of the response current intensity of 5 mM interference at −0.22 V using amperometry to the response current of glucose at a concentration of 5 mM. The response currents of the interferences are approximately 1% to 4% of glucose, indicating the response current generated by the interferences is insufficient to affect the accuracy of glucose detection. Therefore, the glucose biosensor can detect glucose in the presence of interferences in ISF. Fig. S6B shows the response current of 2 mM glucose solution measured using seven electrodes fabricated using the same method. The relative standard deviation (RSD) of the measured current was 1.46%, which means that the fabricated SAN/GOx-modified SPEs have good reproducibility. Fig. S6C also shows the response current of 2 mM glucose solution measured using SAN/GOx-modified SPEs after 0, 7, 14, 21, 28 and 35 days of storage at room temperature. Most previously reported glucose sensors show significant performance degradation within 7 to 30 days of storage.[61,64–66] In contrast, the SAN/GOx-modified SPEs were able to retain about 94.5% of their response current after 35 days of storage at room temperature, demonstrating the remarkable long-term stability of Fe–N–C SANs.

Fabrication and characterization of an HMN patch

An HMN array was fabricated with an Anycubic SLA printer, which has an XY resolution of 16.8 × 24.8 μm. As shown in Fig. 3A and Fig. S7, the HMN array was composed of a 5 × 5 HMN array (12 × 12 × 1.5 mm, $L \times W \times H$) with side openings (hole diameter of 0.16 mm) and through-microchannels (diameter of 0.6 mm). The base diameter, tip diameter, wall thickness and length of each HMN were 750 μm, 100 μm, 75 μm and 1000 μm, respectively. The center-to-center interspacing between HMN tips was optimized to 2 mm for optimal skin permeability and a reduction of insertion force.[67–69] For superior sharpness and dimensional accuracy, the HMN patch was printed with a 45° print angle along X and Y axes, with the side opening of the HMNs facing downward.[70,71] The SEM image, shown in Fig. 3A, depicts the morphology of the printed HMNs.

To visualize the stress distribution of the compression tests, finite element analysis (FEA) of a single HMN was performed *via* Ansys 2024 R2 using the CAD model with a load force of 2 N on the tip surface. The estimated values of the commercial bio resin parameters were 1150 kg m^{-3} for density, 0.35 for Poisson's ratio, and 3.78 × 10^9 Pa for Young's modulus, respectively. The resultant equivalent von-Mises stress is depicted in Fig. 3B, indicating that the highest stress concentration occurred at the tip of the MN (estimated around 2.14 × 10^8 Pa) and gradually decreased along the shaft.[72]

Penetrating the stratum corneum of human skin requires a minimum insertion force of 0.08 N per needle.[73] To investigate its mechanical robustness, compression tests were conducted by applying a force of 50 N. The SEM image in Fig. 3C suggested that the MNs maintained overall structural integrity with only minimal and non-fracture deformation after penetration tests, confirming that each needle can withstand at least 2 N without fracture. Under the given force load, the

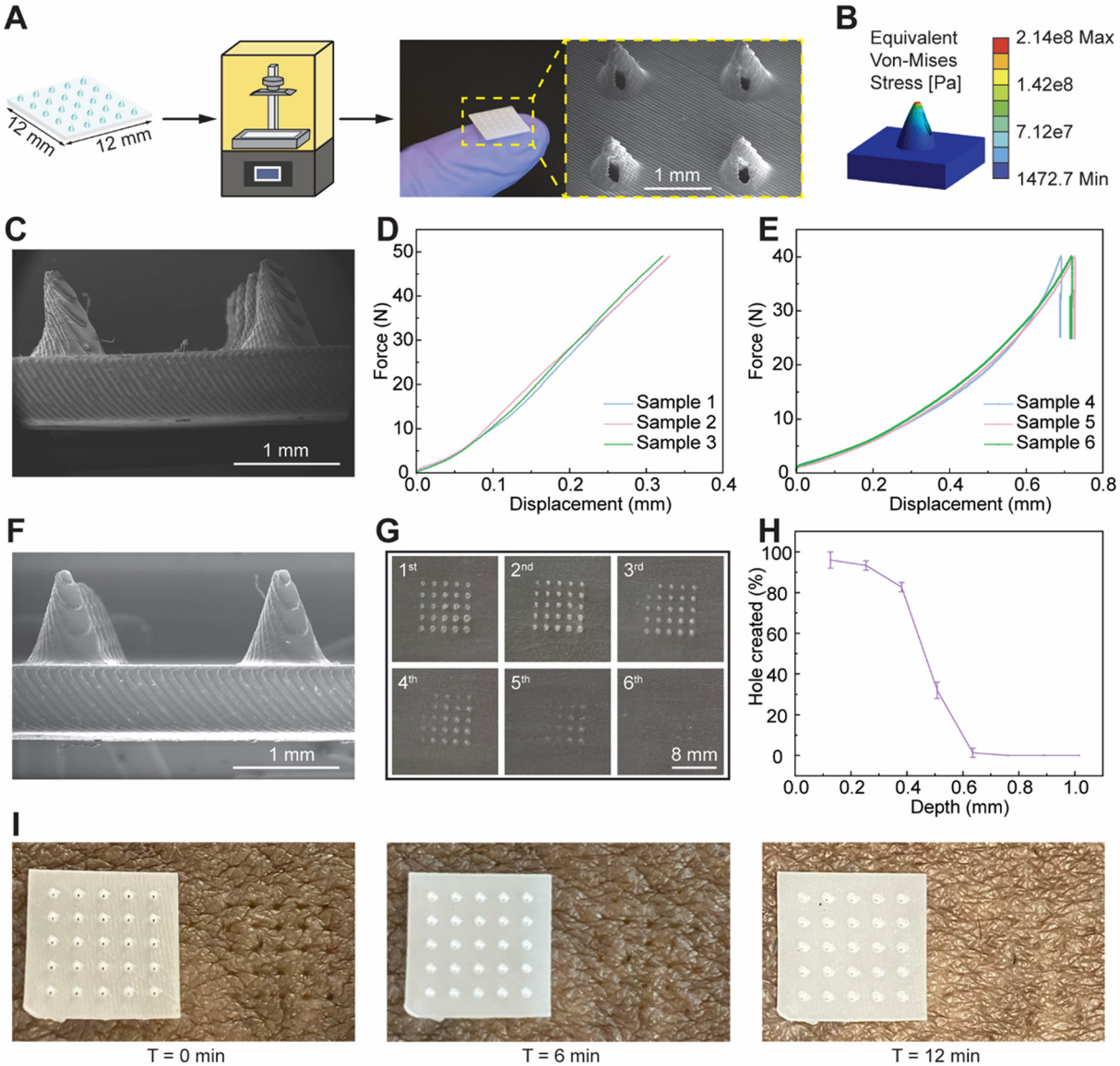

Fig. 3 Fabrication and characterization of the HMN patch. (A) Fabrication process and SEM of HMNs; (B) FEA of HMNs after compression; (C) SEM of HMNs after the compression test; (D) compression results of HMNs; (E) penetration results of parafilm penetration tests; (F) SEM of HMNs after parafilm penetration tests; (G) optical photos of the hole created on the parafilm (from the 1st layer to the 6th layer); (H) penetration efficiency of the HMNs on the parafilm; and (I) time-lapse images of porcine skin after MN array insertion. Images were taken at 0, 6 and 12 min after insertion.

deformation was manifested towards the side with a hollow hole without any fracture, which was consistent with the FEA result. The MNs exhibited a height reduction of 2.55 ± 0.84% after the penetration tests. The recorded force–displacement curve for Samples 1–3 (Fig. 3D) demonstrates that the whole compression process was kept in the elastic region, assuring that the HMNs did not fail during the compression experiments. The penetration performance and depth of the HMNs were subsequently assessed on Samples 4–6 using parafilm penetration tests.[44] A force load was applied at a speed of 1 mm min^{-1} and removed when the resistance reached 40 N and then held for 30 s.[45] The deformation resistance gradually decreased to approximately 25 N (Fig. 3E). After the separation of HMNs, the SEM image (Fig. 3F) of the HMNs and the optical images of the parafilm layers (Fig. 3G, from the 1st layer to the 6th layer) were obtained. The penetration efficiency was analyzed according to the holes created on each parafilm layer and the results are shown in Fig. 3H. It can be concluded that 82.67 ± 1.89% of the fabricated HMNs were able to pierce about 3 layers of parafilm, confirming the successful penetration of HMNs into the dermis layer for ISF sampling.[74] To further evaluate the mechanical behavior and insertion effect of the MN array, we performed a time-lapse observation of porcine skin after MN insertion using the same experimental

setup as the parafilm penetration test. Images were captured every 2 min for a total of 12 min. Images at 0, 6 and 12 min after insertion are shown in Fig. 3I, while images at other time points are provided in Fig. S8. Although the skin surface partially recovered due to its elastic nature, persistent skin deformation and dimpling at the insertion sites were clearly observed over time, indicating localized mechanical disruption. Based on the visible imprint pattern, most of the MNs exhibited successful insertion into the dermal layer to access ISF. Comparable post-insertion skin images have been reported in previous studies employing MNs with similar shapes and lengths to those in the present study, where skin penetration and ISF access were demonstrated.[75,76] As shown in Fig. 3I and Fig. S8, the puncture sites gradually became less visible, indicating the minimally invasive nature of the MNs. Thus, the 3D-printed HMNs demonstrated significant mechanical stability and penetration performance for ISF sampling.

Validation of the integrated sensor on a skin-mimicking phantom gel *in vitro*

Glucose sensing was performed in simulated artificial ISF and the accuracy of the detection was verified using a SAN/GOx-modified SPE. The ISF formula from previous studies was slightly modified to prepare artificial ISF for glucose sensing tests.[50] Parafilm and an agarose hydrogel were used to mimic human skin.[27] The schematic diagram of the detection of simulated skin ISF and the optical image of the detection device is shown in Fig. 4A. The device includes an HMN array, a soft, flexible pump and a SAN/GOx-modified SPE. Fig. 4B illustrates the process for measuring glucose concentration in ISF within a skin-mimicking model. The HMNs penetrated the parafilm to absorb the ISF in the skin-mimicking model for glucose detection, with the flexible pump providing negative pressure for ISF extraction. The SAN/GOx-modified SPE for

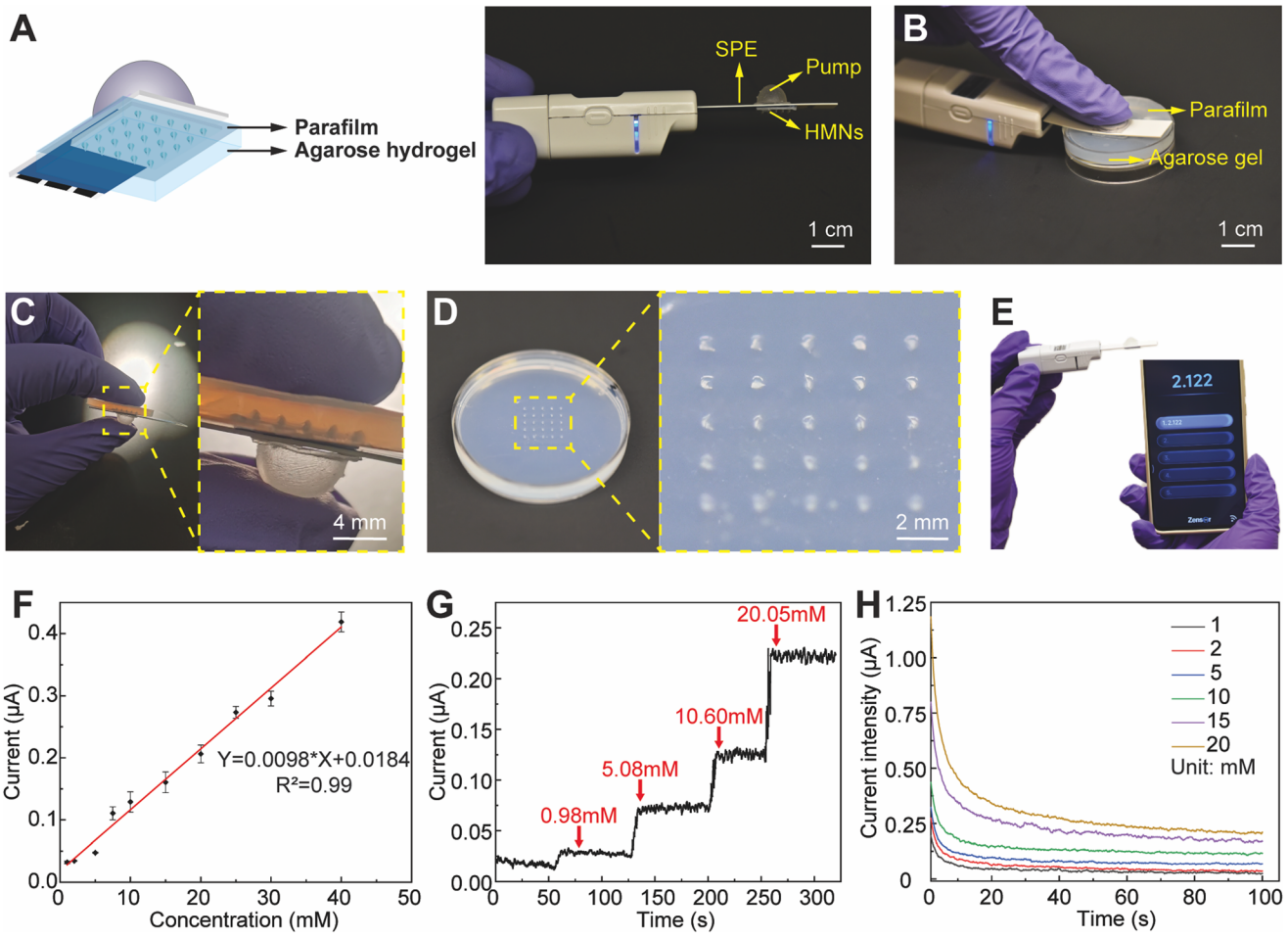

Fig. 4 Glucose detection in artificial ISF and a skin-mimicking phantom gel. (A) Schematic diagram of glucose detection using the SAN/GOx-modified SPE sensor in the skin-mimicking model (left) and assembly of the SAN/GOx-modified SPE sensor (right); (B) glucose sensing operation process in the skin-mimicking model; (C) MN array inserted into the skin-mimicking model; (D) MN array on the hydrogel in the skin-mimicking model after detection; (E) the smartphone application used to display the glucose concentration measured using a glucose sensor; (F) standard curve of current and glucose concentration in artificial ISF using an EIS potentiostat. Data are shown as mean ± SD (n = 3); (G) chronoamperogram for sensing glucose in artificial ISF using an EIS potentiostat; and (H) chronoamperogram for sensing glucose in the skin-mimicking model using an EIS potentiostat.

glucose sensing was connected to a wireless AC impedance/electrochemical impedance spectroscopy (EIS) potentiostat/EIWP110 to analyze the response current from the SPE. Fig. 4C shows the MNs inserted into the hydrogel and successfully extracted ISF. After the removal of the parafilm layer, the remaining holes in the agarose hydrogel are shown in Fig. 4D, demonstrating that the HMNs can pierce the parafilm layer and extract ISF from the hydrogel. The response current was analyzed using an EIS potentiostat, and the detection concentration of the biomarker was rapidly transmitted wirelessly and displayed remotely on a smartphone application, as shown in Fig. 4E. Therefore, the detection method greatly reduces the time required to obtain glucose levels, allowing for a quick response. The HMN array can extract approximately 10–15 μL of liquid from the agarose hydrogel, which is sufficient to meet the required volume (8–10 μL) for electrochemical detection. Fig. 4F shows the curve of current and glucose concentration obtained from the glucose sensor at different glucose concentrations in artificial ISF. The settings of EWIP110 software are shown in Fig. S1A and the responding current curves are shown in Fig. S1B. Within the detection range, a linear relationship between the glucose concentration and response current was observed from 1 mM to 40 mM, following the equation, $Y(\mu A) = 0.0098 \times X(mM) + 0.0184$ and an R^2 value of 0.99. The curve was used as the standard curve for subsequent testing and the equation was entered into the software, as shown in Fig. S1C. The continuous detection curve for glucose in artificial ISF is shown in Fig. 4G. The concentrations of glucose for continuous detection were 0.98, 5.08, 10.6 and 20.05 mM. Through the addition of glucose ISF solution, the response current increased rapidly and then the current value was stabilized. The results indicate that the glucose electrochemical sensor can continuously and rapidly measure the glucose concentration in artificial ISF. Fig. 4H shows the chronoamperogram of glucose detection in a skin-mimicking model. The detection concentrations were 1, 2, 5, 10, 15 and 20 mM, respectively. As the increase of the glucose concentration in ISF, the response current increased progressively. When a time range was selected, the software would calculate the average current during this time and transfer current to concentration through the previously entered standard curve equation and transmit it wirelessly to the smartphone app. To further validate the glucose sensor detection performance, the detection results from the sensor were compared to the reference values of glucose concentration in artificial ISF and the skin-mimicking model, as shown in Table S3. The glucose recoveries from artificial ISF and the skin-mimicking model were approximately 102%–104% and 97%–105%, respectively, demonstrating that the proposed sensor can accurately measure the glucose concentration in a simulated ISF environment. Compared to previous sensors with a limited transmission distance, the proposed sensor achieves a reliable wireless range of 20 m, providing greater mobility and flexibility to users. Therefore, the device combines an HMN-based SAN/GOx-modified SPE with an EIS potentiostat to achieve real-time and continuous glucose monitoring in ISF in a skin-mimicking model by changing the time range.

The sampling stability and repeatability of the 3D-printed electrochemical biosensing platform were evaluated, and the results are provided in the SI. Fig. S9A and B present the images of the finger-activated pump before use and after 100 extraction cycles. No damage in shape, appearance, or actuation performance was observed after repeated operation, indicating that the pump maintains stable mechanical integrity and can withstand long-term cycling use. The pump extraction procedure is shown in Movie S1, which demonstrates that the pump can be easily actuated and rapidly recovers its original shape, supporting its reliability for continuous extraction. In addition, the extraction volume per actuation is summarized in Fig. S9C. The volume ranges from 9.4 to 15.1 μL across 30 sequential cycles, which is sufficient to meet the biosensing volume requirement and confirms the capability for repeated sampling.

Compared with previously reported MN-based sensors, our platform addresses several key limitations. Prior MN-based sensors often rely on multi-step lithography, silicon etching, or PDMS micromolding, which result in high fabrication cost and limited structural tunability.[77–79] For example, silicon etching MNs require multiple complex steps, including wafer spin-coating, photoresist patterning, silicon dioxide etching, and wet etching. These fabrication routes depend on multiple expensive instruments and prolonged processing, which significantly increase the production cost and reduce scalability.[78] PDMS-based MN arrays also involve silicon mold fabrication, PDMS shape-transfer twice and encapsulation.[79] In contrast, 3D printing enables rapid, low-cost production of HMNs with controlled geometry, improving uniformity and scalability for future manufacturing. Furthermore, the Fe–N–C SANs employed in this work address the inherent limitations of natural enzyme-based MN sensors, such as degradation and narrow operational stability.[38,58] The Fe–C–N SANs developed in this study provide durable catalytic activity for long-term storage and monitoring, compared to reported MN-based sensors. In addition, previously reported MN-based sensors typically require benchtop potentiostats and wired connections, limiting their portability and suitability for practical wearable applications.[80,81] In contrast, the wireless module integrated in the present biosensing platform enables real-time glucose readout through a smartphone interface, greatly enhancing portability and user comfort.

Conclusion

This study successfully demonstrated a SAN-functionalized, 3D-printed HMN-based electrochemical sensor for wireless, continuous and real-time glucose monitoring in ISF. The HMNs were fabricated using an affordable desktop 3D printer, underscoring its potential for low-cost and rapid prototyping. The integration of HMNs and a finger-activated, soft, flexible

pump exhibits the potential for minimally invasive sampling of ISF. The SAN-boosted electrochemical sensor exhibited high sensitivity and remarkable selectivity, while the wireless potentiostat enabled user-friendly, real-time, and continuous monitoring of glucose levels. In the proof-of-concept, a skin-mimicking model was used to validate the electrochemical sensing capability and sensitivity. Our integrated wearable sensor provides a feasible solution for continuous and precise glucose monitoring, representing the potential for health monitoring. Future studies will focus on extending the validation to *in vivo* animal models to evaluate ISF extraction efficiency, real-time monitoring performance, and biocompatibility, including potential inflammatory responses. Upon successful preclinical validation, we plan to translate this platform for human testing with appropriate ethical approvals. Additional efforts will also intend to refine fabrication techniques to develop miniaturized devices and optimize material properties for enhanced sensing performance. Moreover, we aim to expand our device's capabilities to monitor multiple biomarkers for comprehensive health management. With these advancements, we believe that our work is promising to notably contribute to the development of next-generation wearable devices, paving the way for personalized healthcare.

Author contributions

Chuchu Chen: writing – original draft, methodology, investigation, and data curation. Yonghao Fu: writing – original draft, methodology, investigation, and data curation. Yuehe Lin: writing – review & editing, supervision, methodology, and conceptualization. Yun Liu: writing – review & editing, supervision, methodology, and conceptualization. Dan Du: writing – review & editing, supervision, methodology, and conceptualization. Kaiyan Qiu: writing – review & editing, supervision, methodology, and conceptualization.

Conflicts of interest

The authors declare no conflicts of interest.

Data availability

Data will be made available upon request from the authors.

Supplementary Information (SI) is available and includes 9 figures, 3 tables, and 1 video: software settings of the EIWP-110 system (Fig. S1); enzyme activity characteristics of Fe-N-C SANs (Fig. S2); electrochemical properties of Fe-N-C SANs (Fig. S3–S5); anti-interference performance, reproducibility, and stability of SAN/GOx-coated SPEs (Fig. S6); dimensional specifications of MN (Fig. S7); time-lapse images of porcine skin after MN insertion (Fig. S8); stability evaluation of the finger-activated pump (Fig. S9); comparison of the detection performance of the HMN-based SAN/GOx-modified glucose sensor with previously reported glucose sensors (Tables S1 and S2); detection results in artificial ISF and a skin-mimicking model (Table S3); and a demonstrating the finger-activated pump extraction process (Movie S1). See DOI: https://doi.org/10.1039/d5an01058f.

Acknowledgements

Prof. Kaiyan Qiu acknowledges Startup Funds and Commercialization Special Project Funds from Washington State University, and the National Science Foundation (DGE #2244082). Prof. Dan Du acknowledges the Centers for Disease Control and Prevention/National Institute for Occupational Safety and Health (CDC/NIOSH) grant (1 R01OH012579-01-00). Prof. Yun Liu acknowledges the funding support from the Australian Research Council (FL210100017). The authors are thankful for the characterization support from the Franceschi Microscopy and Imaging Center (FMIC) at Washington State University.

References

1 A. T. Kharroubi and H. M. Darwish, *World J. Diabetes*, 2015, **6**, 850.
2 Y. Mukhtar, A. Galalain and U. Yunusa, *Eur. J. Biol.*, 2020, **5**, 1–14.
3 R. Eivazzadeh-Keihan, E. Bahojb Noruzi, E. Chidar, M. Jafari, F. Davoodi, A. Kashtiaray, M. Ghafori Gorab, S. Masoud Hashemi, S. Javanshir, R. Ahangari Cohan, A. Maleki and M. Mahdavi, *Chem. Eng. J.*, 2022, **442**, 136183.
4 I. Lee, D. Probst, D. Klonoff and K. Sode, *Biosens. Bioelectron.*, 2021, **181**, 113054.
5 D. C. Klonoff, D. Ahn and A. Drincic, *Diabetes Res. Clin. Pract.*, 2017, **133**, 178–192.
6 D. Rodbard, *Diabetes Technol. Ther.*, 2016, **18**, S2–S3.
7 M. J. Tierney, J. A. Tamada, R. O. Potts, L. Jovanovic and S. Garg, *Biosens. Bioelectron.*, 2001, **16**, 621–629.
8 J. Wu, Y. Liu, H. Yin and M. Guo, *Am. J. Transl. Res.*, 2023, **15**, 3825–3837.
9 Y. Zou, Z. Chu, J. Guo, S. Liu, X. Ma and J. Guo, *Biosens. Bioelectron.*, 2023, **225**, 115103.
10 I. L. Jernelv, K. Milenko, S. S. Fuglerud, D. R. Hjelme, R. Ellingsen and A. Aksnes, *Appl. Spectrosc. Rev.*, 2019, **54**, 543–572.
11 I. Ahmed, N. Jiang, X. Shao, M. Elsherif, F. Alam, A. Salih, H. Butt and A. K. Yetisen, *Sens. Diagn.*, 2022, **1**, 1098–1125.
12 Z. Pu, X. Zhang, H. Yu, J. Tu, H. Chen, Y. Liu, X. Su, R. Wang, L. Zhang and D. Li, *Sci. Adv.*, 2021, **7**, eabd0199.
13 H. Wang, C. Yao, Z. Liu, X. Wang, Z. Liu, T. Zhang, X. Huang, L. Wang, Y. Wang, G. Xiao, S. Farah, H.-j. Chen and X. Xie, *Adv. Intell. Syst.*, 2025, **7**, 2400547.
14 M. Dervisevic, M. Alba, L. Yan, M. Senel, T. R. Gengenbach, B. Prieto-Simon and N. H. Voelcker, *Adv. Funct. Mater.*, 2022, **32**, 2009850.

15 M. Parrilla, U. Detamornrat, J. Domínguez-Robles, R. F. Donnelly and K. De Wael, *Talanta*, 2022, **249**, 123695.
16 P. Jain, A. M. Joshi, S. P. Mohanty and L. R. Cenkeramaddi, *IEEE Access*, 2024, **12**, 61907–61936.
17 J. Heikenfeld, A. Jajack, B. Feldman, S. W. Granger, S. Gaitonde, G. Begtrup and B. A. Katchman, *Nat. Biotechnol.*, 2019, **37**, 407–419.
18 L. Tang, S. J. Chang, C.-J. Chen and J.-T. Liu, *Sensors*, 2020, **20**, 6925.
19 J. J. García-Guzmán, C. Pérez-Ràfols, M. Cuartero and G. A. Crespo, *TrAC, Trends Anal. Chem.*, 2021, **135**, 116148.
20 M. Friedel, I. A. P. Thompson, G. Kasting, R. Polsky, D. Cunningham, H. T. Soh and J. Heikenfeld, *Nat. Biomed. Eng.*, 2023, **7**, 1541–1555.
21 H. Teymourian, F. Tehrani, K. Mahato and J. Wang, *Adv. Healthcare Mater.*, 2021, **10**, 2002255.
22 T. Abbasiasl, F. Mirlou, H. Mirzajani, M. J. Bathaei, E. Istif, N. Shomalizadeh, R. E. Cebecioğlu, E. E. Özkahraman, U. C. Yener and L. Beker, *Adv. Mater.*, 2024, **36**, 2304704.
23 L. Bao, J. Park, G. Bonfante and B. Kim, *Drug Delivery Transl. Res.*, 2022, **12**, 395–414.
24 K. Lee, M. J. Goudie, P. Tebon, W. Sun, Z. Luo, J. Lee, S. Zhang, K. Fetah, H.-J. Kim, Y. Xue, M. A. Darabi, S. Ahadian, E. Sarikhani, W. Ryu, Z. Gu, P. S. Weiss, M. R. Dokmeci, N. Ashammakhi and A. Khademhosseini, *Adv. Drug Delivery Rev.*, 2020, **165–166**, 41–59.
25 R. Jamaledin, C. K. Y. Yiu, E. N. Zare, L.-N. Niu, R. Vecchione, G. Chen, Z. Gu, F. R. Tay and P. Makvandi, *Adv. Mater.*, 2020, **32**, 2002129.
26 Y. Liu, Q. Yu, X. Luo, L. Yang and Y. Cui, *Microsyst. Nanoeng.*, 2021, **7**, 1–12.
27 H. Teymourian, C. Moonla, F. Tehrani, E. Vargas, R. Aghavali, A. Barfidokht, T. Tangkuaram, P. P. Mercier, E. Dassau and J. Wang, *Anal. Chem.*, 2020, **92**, 2291–2300.
28 X. Jiang, E. C. Wilkirson, A. O. Bailey, W. K. Russell and P. B. Lillehoj, *Cell Rep. Phys. Sci.*, 2024, **5**, 101975.
29 P. P. Samant, M. M. Niedzwiecki, N. Raviele, V. Tran, J. Mena-Lapaix, D. I. Walker, E. I. Felner, D. P. Jones, G. W. Miller and M. R. Prausnitz, *Sci. Transl. Med.*, 2020, **12**, eaaw0285.
30 L. Gao, J. Zhuang, L. Nie, J. Zhang, Y. Zhang, N. Gu, T. Wang, J. Feng, D. Yang, S. Perrett and X. Yan, *Nat. Nanotechnol.*, 2007, **2**, 577–583.
31 Q. Tian, S. Li, Z. Tang, Z. Zhang, D. Du, X. Zhang, X. Niu and Y. Lin, *Adv. Healthcare Mater.*, 2025, **14**, 2401630.
32 N. Cheng, J.-C. Li, D. Liu, Y. Lin and D. Du, *Small*, 2019, **15**, 1901485.
33 M. Liu, W. Xu, Y. Tang, Y. Wu, W. Gu, D. Du, Y. Lin and C. Zhu, *Angew. Chem., Int. Ed.*, 2025, **64**, e202424070.
34 W. Wu, L. Huang, E. Wang and S. Dong, *Chem. Sci.*, 2020, **11**, 9741–9756.
35 W. Xu, Y. Wu, W. Gu, D. Du, Y. Lin and C. Zhu, *Chem. Soc. Rev.*, 2024, **53**, 137–162.
36 L. Jiao, W. Xu, Y. Wu, H. Yan, W. Gu, D. Du, Y. Lin and C. Zhu, *Chem. Soc. Rev.*, 2021, **50**, 750–765.
37 S. Ding, J. A. Barr, Z. Lyu, F. Zhang, M. Wang, P. Tieu, X. Li, M. H. Engelhard, Z. Feng, S. P. Beckman, X. Pan, J.-C. Li, D. Du and Y. Lin, *Adv. Mater.*, 2024, **36**, 2209633.
38 C. Chen, Y. Fu, S. S. Sparks, Z. Lyu, A. Pradhan, S. Ding, N. Boddeti, Y. Liu, Y. Lin, D. Du and K. Qiu, *ACS Sens.*, 2024, **9**, 3212–3223.
39 Z. Lyu, S. Ding, P. Tieu, L. Fang, X. Li, T. Li, X. Pan, M. H. Engelhard, X. Ruan, D. Du, S. Li and Y. Lin, *Research*, 2022, **2022**, 9823290.
40 X. Niu, Q. Shi, W. Zhu, D. Liu, H. Tian, S. Fu, N. Cheng, S. Li, J. N. Smith, D. Du and Y. Lin, *Biosens. Bioelectron.*, 2019, **142**, 111495.
41 M. Parrilla, A. Sena-Torralba, A. Steijlen, S. Morais, Á. Maquieira and K. De Wael, *Biosens. Bioelectron.*, 2024, **251**, 116131.
42 M. Parrilla, A. Steijlen, R. Kerremans, J. Jacobs, L. den Haan, J. De Vreese, Y. Van Noten Géron, P. Clerx, R. Watts and K. De Wael, *Chem. Eng. J.*, 2024, **500**, 157254.
43 A. Sena-Torralba, M. Parrilla, A. Hernanz-Grimalt, A. Steijlen, E. Ortiz-Zapater, C. Cabaleiro-Otero, N. López-Riquelme, S. Cerveró-Ferragut, Á. Maquieira, K. De Wael and S. Morais, *Anal. Chem.*, 2024, **96**, 20684–20692.
44 B. H. Alrimawi, J. Y. Lee, K. W. Ng and C. F. Goh, *RSC Pharm.*, 2024, **1**, 227–233.
45 E. Larrañeta, J. Moore, E. M. Vicente-Pérez, P. González-Vázquez, R. Lutton, A. D. Woolfson and R. F. Donnelly, *Int. J. Pharm.*, 2014, **472**, 65–73.
46 A. H. Sabri, Z. Cater, J. Ogilvie, D. J. Scurr, M. Marlow and J. Segal, *J. Drug Delivery Sci. Technol.*, 2020, **58**, 101766.
47 S. Fu, C. Zhu, D. Su, J. Song, S. Yao, S. Feng, M. H. Engelhard, D. Du and Y. Lin, *Small*, 2018, **14**, 1703118.
48 B. Jiang, D. Duan, L. Gao, M. Zhou, K. Fan, Y. Tang, J. Xi, Y. Bi, Z. Tong, G. F. Gao, N. Xie, A. Tang, G. Nie, M. Liang and X. Yan, *Nat. Protoc.*, 2018, **13**, 1506–1520.
49 J.-J. Zheng, F. Zhu, N. Song, F. Deng, Q. Chen, C. Chen, J. He, X. Gao and M. Liang, *Nat. Protoc.*, 2024, **19**, 3470–3488.
50 P. Bollella, S. Sharma, A. E. G. Cass and R. Antiochia, *Electroanalysis*, 2019, **31**, 374–382.
51 A. H. Bretag, *Life Sci.*, 1969, **8**, 319–329.
52 S. R. Chinnadayyala, J. Park, A. T. Satti, D. Kim and S. Cho, *Electrochim. Acta*, 2021, **369**, 137691.
53 S. H. Tawakey, M. Mansour, A. Soltan and A. I. Salim, *Lab Chip*, 2024, **24**, 3958–3972.
54 K. Y. Goud, K. Mahato, H. Teymourian, K. Longardner, I. Litvan and J. Wang, *Sens. Actuators, B*, 2022, **354**, 131234.
55 C. Zhao, C. Xiong, X. Liu, M. Qiao, Z. Li, T. Yuan, J. Wang, Y. Qu, X. Wang, F. Zhou, Q. Xu, S. Wang, M. Chen, W. Wang, Y. Li, T. Yao, Y. Wu and Y. Li, *Chem. Commun.*, 2019, **55**, 2285–2288.
56 X. Niu, X. Li, Z. Lyu, J. Pan, S. Ding, X. Ruan, W. Zhu, D. Du and Y. Lin, *Chem. Commun.*, 2020, **56**, 11338–11353.
57 L. Jiao, W. Xu, H. Yan, Y. Wu, C. Liu, D. Du, Y. Lin and C. Zhu, *Anal. Chem.*, 2019, **91**, 11994–11999.

58 Z. Lyu, S. Ding, N. Zhang, Y. Zhou, N. Cheng, M. Wang, M. Xu, Z. Feng, X. Niu, Y. Cheng, C. Zhang, D. Du and Y. Lin, *Research*, 2020, **2020**, 4724505.
59 S. H. Khatami, O. Vakili, N. Ahmadi, E. Soltani Fard, P. Mousavi, B. Khalvati, A. Maleksabet, A. Savardashtaki, M. Taheri-Anganeh and A. Movahedpour, *Biotechnol. Appl. Biochem.*, 2022, **69**, 939–950.
60 M. Thompson, S. L. R. Ellison and R. Wood, *Pure Appl. Chem.*, 2002, **74**, 835–855.
61 Z. Xu, Q. Wang, H. Zhangsun, S. Zhao, Y. Zhao and L. Wang, *Food Chem.*, 2021, **349**, 129202.
62 A. G. Ayankojo, J. Reut, V. Ciocan, A. Öpik and V. Syritski, *Talanta*, 2020, **209**, 120502.
63 Y. Yao, J. Chen, Y. Guo, T. Lv, Z. Chen, N. Li, S. Cao, B. Chen and T. Chen, *Biosens. Bioelectron.*, 2021, **179**, 113078.
64 T. S. Gopal, S. K. Jeong, T. A. Alrebdi, S. Pandiaraj, A. Alodhayb, M. Muthuramamoorthy and G. Andrews Nirmala, *Mater. Today Chem.*, 2022, **24**, 100891.
65 C. Kong, L. Tang, X. Zhang, S. Sun, S. Yang, X. Song and Z. Yang, *J. Mater. Chem. A*, 2014, **2**, 7306–7312.
66 X. Gou, S. Sun, Q. Yang, P. Li, S. Liang, X. Zhang and Z. Yang, *New J. Chem.*, 2018, **42**, 6364–6369.
67 V. Ebrahiminejad, P. D. Prewett, G. J. Davies and Z. Faraji Rad, *Adv. Mater. Interfaces*, 2022, **9**, 2101856.
68 E. L. Zoudani, N.-T. Nguyen and N. Kashaninejad, *Small Struct.*, 2024, 2400121, DOI: 10.1002/sstr.202400121.
69 I. Xenikakis, K. Tsongas, E. K. Tzimtzimis, O. L. Katsamenis, E. Demiri, C. K. Zacharis, D. Georgiou, E. P. Kalogianni, D. Tzetzis and D. G. Fatouros, *J. Drug Delivery Sci. Technol.*, 2022, **67**, 102891.
70 J. M. Loh, Y. J. L. Lim, J. T. Tay, H. M. Cheng, H. L. Tey and K. Liang, *Bioact. Mater.*, 2024, **32**, 222–241.
71 M. Razzaghi, J. A. Ninan, M. Azimzadeh, E. Askari, A. H. Najafabadi, A. Khademhosseini and M. Akbari, *Adv. Healthcare Mater.*, 2024, **13**, 2400881.
72 C. Yeung, S. Chen, B. King, H. Lin, K. King, F. Akhtar, G. Diaz, B. Wang, J. Zhu, W. Sun, A. Khademhosseini and S. Emaminejad, *Biomicrofluidics*, 2019, **13**, 064125.
73 S. P. Davis, B. J. Landis, Z. H. Adams, M. G. Allen and M. R. Prausnitz, *J. Biomech.*, 2004, **37**, 1155–1163.
74 X. Zhang, W. Zhang, W. Wu and J. Chen, *Microchem. J.*, 2023, **195**, 109477.
75 Z. Chen, Y. Guo, X. Gu, X. Liu, J. Zhang, C. Song and L. Wang, *Microchem. J.*, 2024, **206**, 111546.
76 M. Parrilla, A. Vanhooydonck, M. Johns, R. Watts and K. De Wael, *Sens. Actuators, B*, 2023, **378**, 133159.
77 L. Ren, Q. Jiang, Z. Chen, K. Chen, S. Xu, J. Gao and L. Jiang, *Sens. Actuators, A*, 2017, **268**, 38–45.
78 O. Howells, G. J. Blayney, B. Gualeni, J. C. Birchall, P. F. Eng, H. Ashraf, S. Sharma and O. J. Guy, *Eur. J. Pharm. Biopharm.*, 2022, **171**, 19–28.
79 R. Wang, J. Bai, X. Zhu, Z. Li, L. Cheng, G. Zhang and W. Zhang, *Biomed. Microdevices*, 2022, **24**, 27.
80 J. Gao, W. Huang, Z. Chen, C. Yi and L. Jiang, *Sens. Actuators, B*, 2019, **287**, 102–110.
81 C. Thatte, F. Barry, C. Ferreira, E. O'Keeffe, V. Cioce, P. Galvin and S. R. Teixeira, *ACS Omega*, 2025, **10**, 36203–36215.